Neurobiology of Disease

Synapse-Specific Defects in Synaptic Transmission in the Cerebellum of W246G Mutant ELOVL4 Rats–a Model of Human SCA34

Raghavendra Y. Nagaraja,[1,2] Megan A. Stiles,[2] David M. Sherry,[1,3,4] Martin-Paul Agbaga,[1,2] and Mohiuddin Ahmad[1]

[1]Department of Cell Biology, University of Oklahoma Health Sciences Center, Oklahoma City, Oklahoma 73104, [2]Department of Ophthalmology, Dean McGee Eye Institute, University of Oklahoma Health Sciences Center, Oklahoma City, Oklahoma 73104, [3]Department of Neurosurgery, University of Oklahoma Health Sciences Center, Oklahoma City, Oklahoma 73104, and [4]Department of Pharmaceutical Sciences, University of Oklahoma Health Sciences Center, Oklahoma City, Oklahoma 73104

Elongation of very long fatty acids-4 (ELOVL4) mediates biosynthesis of very long chain-fatty acids (VLC-FA; ≥28 carbons). Various mutations in this enzyme result in spinocerebellar ataxia-34 (SCA34). We generated a rat model of human SCA34 by knock-in of a naturally occurring c.736T>G, p.W246G mutation in the *Elovl4* gene. Our previous analysis of homozygous W246G mutant ELOVL4 rats (MUT) revealed early-onset gait disturbance and impaired synaptic transmission and plasticity at parallel fiber-Purkinje cell (PF-PC) and climbing fiber-Purkinje cell (CF-PC) synapses. However, the underlying mechanisms that caused these defects remained unknown. Here, we report detailed patch-clamp recordings from Purkinje cells that identify impaired synaptic mechanisms. Our results show that miniature EPSC (mEPSC) frequency is reduced in MUT rats with no change in mEPSC amplitude, suggesting a presynaptic defect of excitatory synaptic transmission on Purkinje cells. We also find alterations in inhibitory synaptic transmission as miniature IPSC (mIPSC) frequency and amplitude are increased in MUT Purkinje cells. Paired-pulse ratio is reduced at PF-PC synapses but increased at CF-PC synapses in MUT rats, which along with results from high-frequency stimulation suggest opposite changes in the release probability at these two synapses. In contrast, we identify exaggerated persistence of EPSC amplitude at CF-PC and PF-PC synapses in MUT cerebellum, suggesting a larger readily releasable pool (RRP) at both synapses. Furthermore, the dendritic spine density is reduced in MUT Purkinje cells. Thus, our results uncover novel mechanisms of action of VLC-FA at cerebellar synapses, and elucidate the synaptic dysfunction underlying SCA34 pathology.

Key words: **cerebellum; Elongation of very long fatty acids-4; Purkinje cells; spinocerebellar ataxia-34; synaptic transmission**

Significance Statement

Very long chain-fatty acids (VLC-FA) are an understudied class of fatty acids that are present in the brain. They are critical for brain function as their deficiency caused by mutations in elongation of very long fatty acids-4 (ELOVL4), the enzyme that mediates their biosynthesis, results in neurologic diseases including spinocerebellar ataxia-34 (SCA34), neuroichthyosis, and Stargardt-like macular dystrophy. In this study, we investigated the synaptic defects present in a rat model of SCA34 and identified defects in presynaptic neurotransmitter release and dendritic spine density at synapses in the cerebellum, a brain region involved in motor coordination. These results advance our understanding of the synaptic mechanisms regulated by VLC-FA and describe the synaptic dysfunction that leads to motor incoordination in SCA34.

Received Mar. 1, 2023; revised June 30, 2023; accepted July 20, 2023.

Author contributions: D.M.S., M.-P.A., and M.A. designed research; R.Y.N. and M.A.S. performed research; R.Y.N., M.A.S., D.M.S., and M.A. analyzed data; M.A. wrote the first draft of the paper; R.Y.N., D.M.S., M.-P.A., and M.A. edited the paper; M.A. wrote the paper.

This study and the authors were supported by the National Eye Institute/National Institutes of Health (NIH) Grant R01 EY030513 (to M.-P.A.), the National Institute of Arthritis and Musculoskeletal and Skin Diseases/NIH Grant R21-AR076035 (to M.-P.A.), the National Institute of Mental Health/NIH Grant R01 MH125998 (to M.A.), a Multi-PI Team Science grant from Presbyterian Health Foundation (D.M.S., M.-P.A. and M.A.), the Whitehall Foundation Grant 2021-08-077 (to M.A.), a shared equipment grant from Presbyterian Health Foundation (D.M.S.), and support from the University of Oklahoma Health Sciences Center Department of Cell Biology. Research reported here was also supported in part by the National Institute of General Medical Sciences Grant P20 GM125528, the Cellular and Molecular Geroscience CoBRE Grant awarded to the University of Oklahoma (P30 EY021725), and unrestricted grant support from Research to Prevent Blindness to the Department of Ophthalmology of the Dean McGee Eye Institute. We thank Vicki Ea, Joel McRae, Mark Dittmar, and the staff of the Dean McGee Eye Institute Animal Research Facility for taking care of the animals and Fatemeh Shariati of the University of Oklahoma Vision Genotyping Core for genotyping.

The authors declare no competing financial interests.

Correspondence should be addressed to Mohiuddin Ahmad at mohiuddin-ahmad@ouhsc.edu.

https://doi.org/10.1523/JNEUROSCI.0378-23.2023

Introduction

Lipids are critical to the health of the central nervous system and defects in neuronal lipid metabolism and function lead to a variety of neurologic diseases (Adibhatla and Hatcher, 2007; Di Paolo and Kim, 2011; Hussain et al., 2019; Alessenko and Albi, 2020). Despite their importance, our understanding of the roles of diverse classes of lipids (Fitzner et al., 2020) in regulating brain structure and function remains sparse. In particular, little is known about the function of very long chain-saturated and polyunsaturated fatty acids (VLC-SFA and VLC-PUFA), which have chain lengths of 28 carbon atoms or more (Deák et al., 2019; Yeboah et al., 2021). Elongation of very long fatty acids-4 (ELOVL4) is the enzyme that is responsible for catalyzing the rate-limiting step in the biosynthesis of both VLC-SFA and VLC-PUFA (Agbaga et al., 2008). ELOVL4 has a restricted expression in the body, being present only in the brain, retina, skin, Meibomian glands and testes, where it generates a tissue-specific pattern of VLC-SFA and VLC-PUFA (Sherry et al., 2017; Hopiavuori et al., 2019; Yeboah et al., 2021).

The importance of ELOVL4 and its products is underscored by the findings that three distinct groups of mutations in the *ELOVL4* gene cause three distinct neurologic diseases. Homozygous inheritance of recessive mutations that lead to truncation of the ELOVL4 protein cause a neuro-ichthyotic syndrome characterized by severe seizures, intellectuality disability, and childhood death (Aldahmesh et al., 2011; Mir et al., 2014). Heterozygous ELOVL4 mutations that remove the ER retention signal in the enzyme cause autosomal dominant Stargardt-like macular dystrophy (STGD3) resulting in juvenile blindness (Bernstein et al., 2001; Edwards et al., 2001; Zhang et al., 2001). Importantly, heterozygous inheritance of a number of different *ELOVL4* point mutations causes autosomal dominant spinocerebellar ataxia-34 (SCA34), a neurodegenerative disease of the cerebellum (Cadieux-Dion et al., 2014; Ozaki et al., 2015, 2019; Bourque et al., 2018; Xiao et al., 2019; Beaudin et al., 2020). This disease is characterized by age-related progressive gait ataxia that may be accompanied by dysarthria and eye movement abnormalities, with or without erythrokeratitis variabilis (EKV), a disorder of the skin. SCA34 belongs to a large group of spinocerebellar ataxias whose mechanisms remain largely unknown and for which no treatment is currently available (Dueñas et al., 2006).

In order to understand the pathophysiology of SCA34 and to decipher the function of ELOVL4 products in the cerebellum, we recently generated a rodent model of human SCA34 using CRISPR-Cas9 gene editing to introduce the SCA34-causing c.736T>G (p.W246G) mutation in the Long Evans rat genome (Agbaga et al., 2020; Nagaraja et al., 2021). The SCA34 rat recapitulated multiple features of the human disease including motor incoordination and EKV-like skin defects that were already apparent at two months of age (Nagaraja et al., 2021). Field potential recordings revealed robust impairments in basal excitatory synaptic transmission and synaptic plasticity at parallel fiber-Purkinje cell (PF-PC) and climbing fiber-Purkinje cell (CF-PC) synapses (Nagaraja et al., 2021). Interestingly, the cerebellum showed unaltered cytoarchitectural organization with no evidence of degeneration by six months of age. These results suggested that the primary impairment in SCA34 may be synaptic dysfunction before neurodegeneration sets in at advanced age. Although our initial analysis revealed basic defects at Purkinje cell excitatory synapses, the physiological processes that are impaired to cause these synaptic deficits remained unidentified. Here, we have performed detailed patch-clamp recordings in acute cerebellar slices and identified distinct presynaptic and postsynaptic defects at PF-PC, CF-PC and inhibitory synapses. The results reveal that ELOVL4 and its very long chain-fatty acids (VLC-FA) products regulate common and divergent mechanisms involving vesicular release probability, readily releasable pool (RRP), and spine density at synapses formed on Purkinje cells. These findings identify for the first time the mechanistic processes that are impaired to generate defects in synaptic transmission and plasticity reported earlier in the cerebellum of ELOVL4 W246G rats. These results also elucidate Purkinje cell synaptic dysfunction that could produce ataxia in the absence of neurodegeneration in a model of spinocerebellar ataxia.

Materials and Methods

Animals

A CRISPR/Cas9 gene editing approach was used to generate F0 founder Long–Evans rats with heterozygous knock-in of the c.736T>G, p.W246G mutation in the *Elovl4* gene that causes human SCA34 (Ozaki et al., 2015). These founders were bred to wild-type (WT) Long–Evans rats to establish a breeding colony (Agbaga et al., 2020). All experiments were performed using male and female WT and MUT rats, with genotype confirmed by PCR. Rats were maintained in a pathogen-free barrier facility on a 12/12 h light/dark cycle (~25–40 lux at cage level) with food and water available at all times. All animal procedures were approved by the Institutional Animal Care and Use Committee of the University of Oklahoma Health Sciences Center and conformed to the National Institutes of Health *Guide for the Care and Use of Laboratory Animals*, United Stated Public Health Service guidelines, and the Association for Research in Vision and Ophthalmology Resolution on the Use of Animals in Research.

Electrophysiology

Sagittal slices of the cerebellar vermis were prepared from two- to five-month-old Long–Evans rats. Animals were transcardially perfused (following anesthesia with ketamine and dexmedetomidine) with ice-cold dissection buffer containing (in mM): 50 sucrose, 125 NaCl, 25 $NaHCO_3$, 2.5 glucose, 2.5 KCl, 1.25 NaH_2PO_4, 4.9 $MgCl_2$, and 0.1 $CaCl_2$, as described before (Troyano-Rodriguez et al., 2019a). The rats were then decapitated and their brains rapidly removed. Acute cerebellar slices (270 μm thick) were cut on a vibratome (VT1200S, Leica Biosystems) in the dissection buffer, and immediately transferred to an incubation chamber which had artificial CSF (ACSF) containing (in mM): 119 NaCl, 26 $NaHCO_3$, 11 glucose, 2.5 KCl, 1 NaH_2PO_4, 1.3 $MgSO_4$, and 2.5 $CaCl_2$ (Ahmad et al., 2012; Troyano-Rodriguez et al., 2019a,b). The slices were allowed to recover at 32°C for 30 min before incubation at room temperature for a further 1 h. During recordings, the slices were placed in a recording chamber constantly perfused with heated ACSF (29–30°C) and gassed continuously with 95% O_2 and 5% CO_2. The ACSF contained 50 μM picrotoxin during all recordings except when collecting miniature IPSCs (mIPSCs). Tetrodotoxin (TTX; 0.5 μM) was added to the ACSF when recording miniature EPSC (mEPSC) and mIPSC. Whole-cell recording pipettes (2–4 MΩ) were filled with either CsCl or K-gluconate based internal solution. For voltage-clamp recordings, we used an internal solution containing the following (in mM): 135 $CsMeSO_3$, 8 NaCl, 2 $MgCl_2$, 10 HEPES, 0.25 EGTA, 2 Mg_2ATP, 0.3 Na_3GTP, 7 phosphocreatine, and 1 QX-314 chloride (pH 7.28–7.32 adjusted with CsOH; osmolality 298–302 mOsm/kg). For current-clamp recordings, we used an internal solution containing the following (in mM): 135 K-gluconate, 10 HEPES, 10 NaCl, 1 $MgCl_2$, 0.1 BAPTA, 0.1 $CaCl_2$, 2 ATP-Mg, and 10 phosphocreatine (pH 7.28–7.30 adjusted with KOH; osmolality 290–292 mOsm/kg). Purkinje neurons were visualized using infrared differential interference contrast (DIC) on an upright microscope (Olympus BX51WI, Olympus).

To record spontaneous synaptic events, Purkinje cells were held in whole-cell voltage-clamp mode. mEPSCs were recorded while holding the cells at −70 mV and mIPSCs were recorded while holding the cells at 0 mV. To generate evoked EPSCs, a double-barreled glass pipette filled with ACSF was used as a bipolar stimulation electrode. The CF input was activated by placing the stimulation electrode in the granule cell layer, and the PF input was activated in the molecular layer (ML). To

evoke EPSCs, paired pulses (50-ms interpulse interval) were applied to the PF or CF input. The duration of the stimulation pulse was set at 0.1 ms. Whole-cell voltage-clamp recordings were obtained from Purkinje cells, holding the cells at −65 or −70 mV while recording PF-PC EPSCs. CF responses were identified as large all-or-none EPSCs, with paired-pulse depression when stimulated with two pulses 50 ms apart at −65 or −70 mV. Purkinje cells were then held at a holding potential of −10 mV for collecting data on CF-PC EPSCs. The junction potentials were not adjusted. For whole-cell current-clamp recordings, cells were opened in voltage-clamp mode and then switched to current-clamp mode. Slow current injection was applied to keep the membrane potential around −60 mV. For inducing action potentials and depolarization sag, 0.5-s-long depolarizing (100–1000 pA) or 2-s-long hyperpolarizing (−50 to −250 pA) current steps were applied respectively. Data were collected with MultiClamp 700B amplifier (Molecular Devices), filtered with 2 kHz Bessel filter and digitized at 10 kHz with the A/D converter ITC-18 (Instrutech Corporation). Data were acquired and analyzed using a custom-made program written in Igor Pro software (Wavemetrics). The miniature events were identified and analyzed in the Mini Analysis program (SynaptoSoft).

Intracellular dye injection and imaging for dendritic spine analysis

Sagittal slices (200 µm thick) of the cerebellar vermis were prepared from both WT and MUT rats as described above. To visualize dendritic organization and spines on individual Purkinje cells, Purkinje cells were filled with the fluorescent dye Alexa 568 hydrazide (0.5 mM) in whole-cell patch-clamp pipette. The whole-cell access to Purkinje cells was maintained for ~20 min to allow the dye to disperse into the dendritic branches. The dye filling in the Purkinje cells was confirmed using a fluorescence illumination system before the slices were fixed with 4% paraformaldehyde in PBS. Confocal image Z-stacks (Z-stack thickness = 0.05 µm) were captured from across the width of the molecular layer (ML) using a Nikon W1-CSU-SoRa spinning disk confocal microscope and a 60× oil immersion objective (NA 1.40). Each Z-stack of images was compressed as maximum intensity projection and saved as a single TIFF file; 15- to 20-µm-long dendritic segments were selected from tertiary branches of the Purkinje cell dendritic tree for spine counting. Nine dendritic segments per cell were analyzed from each dye injected cell. The number of spines in each segment were counted using *Dendritic Spine Counter* plugin in ImageJ. The spine density was calculated as the ratio of the number of spines and the length of the dendritic segment.

Immunolabeling and imaging for dendritic spine analysis

Freshly isolated cerebella from WT and MUT rats between three and four months of age were fixed using 4% paraformaldehyde in 0.1 M PBS (pH 7.2) and embedded in 7% low melting point agarose. Vibratome sections were prepared from the fixed cerebellar vermis in the sagittal plane at 45-µm thickness. Nonspecific labeling was blocked for 1–2 h at room temperature using "blocking solution" (10% normal goat serum + 5% BSA + 0.1% Triton X-100 in PBS). Blocking solution was removed and sections were incubated in mouse monoclonal anti-calbindin (NeuroMab, University of California, Davis/National Institutes of Health NeuroMab Facility, catalog #75-448; RRID: AB_2686913, diluted 1:500 in blocking solution) at room temperature for 48 h in a humid chamber. Sections were rinsed in PBS at room temperature, then incubated in Goat anti-mouse Fab fragment secondary antiserum conjugated to AlexaFluor 647 (Jackson ImmunoResearch, catalog #115-607-003; RRID:AB_2338931, diluted 1:100 in blocking solution) for 4 h at room temperature. Sections were rinsed in PBS at room temperature, then mounted on a slide in Prolong Glass (Invitrogen, catalog #P36982). Super-resolution confocal image Z-stacks (*z*-axis resolution = 0.02 µm/slice; 2.5–3.0 µm in total thickness) of Calbindin labeling were captured using a Nikon W1-CSU-SoRa spinning disk confocal microscope fitted with a 100× oil immersion objective (NA 1.45) to visualize Purkinje cell dendrites and dendritic spines from across the width of the molecular layer (ML). To determine Purkinje cell dendritic spine density, the number of spines on 10 µm segments of Calbindin-positive dendrites were quantified. Images of cerebellar cortex for analysis were acquired near the middle of lobule 8, which was selected for analysis because of its linear shape. For each specimen, the average spine density (number of spines/10 µm) was calculated from 20–22 independent dendritic segments sampled from across the depth of the ML. Because it was not possible to determine which specific Purkinje cell gave rise to each dendritic segment, each dendritic segment was treated as an independent sample for this analysis.

Statistical analyses

Statistical analysis of electrophysiology and cell filling data were done using Student's unpaired *t* test or two-way ANOVA with Bonferroni's multiple comparison *post hoc* test. For immunohistochemical data, statistical significance was determined using Welch's unpaired two-way *t* test. All statistical analyses were performed in GraphPad Prism 7. Statistical significance was set to $p < 0.05$. Data are displayed as mean ± SEM along with individual values.

Results

The W246G ELOVL4 mutation alters miniature excitatory and inhibitory synaptic currents in Purkinje cells

We performed whole-cell patch-clamp recordings from Purkinje cells in acute cerebellar slices from wild-type (WT) and homozygous ELOVL4 W246G knock-in (MUT) rats. The cerebellar slices were obtained from two- to five-month-old animals as motor impairments and synaptic dysfunction are already present in MUT rats at two months of age (Nagaraja et al., 2021). In order to understand whether the impairment of basal excitatory synaptic transmission onto Purkinje cells reported in our previous study (Nagaraja et al., 2021) was because of presynaptic and/or postsynaptic defects, we recorded miniature EPSCs (mEPSCs) in Purkinje cells in the presence of TTX. We found that the frequency of mEPSC was reduced in MUT Purkinje cells compared with WT (WT 4.46 ± 0.41 Hz, $n = 9$ cells, 4 rats; MUT 2.46 ± 0.32 Hz, $n = 8$ cells, 5 rats; $p = 0.002$; Fig. 1*A*). However, the amplitude of mEPSC was not changed (WT 13.00 ± 1.15 pA, $n = 9$ cells, 4 rats; MUT 12.65 ± 0.89 pA, $n = 8$ cells, 5 rats; $p = 0.820$; Fig. 1*A*). This combination of findings suggests an impairment in presynaptic vesicular glutamate release and/or reduced excitatory synapse number, but no change in postsynaptic AMPA receptor content at functional synapses. We then examined whether inhibitory synaptic transmission onto Purkinje cells, mediated mostly by molecular layer interneurons (MLI), was altered in MUT rats. The frequency of miniature IPSCs (mIPSCs) was increased in MUT Purkinje cells compared with WT (WT 2.37 ± 0.29 Hz, $n = 11$ cells, 3 rats; MUT 4.53 ± 0.62 Hz, $n = 13$ cells, 5 rats; $p = 0.007$; Fig. 1*B*). In addition, the amplitude of mIPSC was also increased in MUT Purkinje cells (WT 14.59 ± 0.79 pA, $n = 11$ cells, 3 rats; MUT 18.10 ± 1.26 pA, $n = 13$ cells, 5 rats; $p = 0.034$; Fig. 1*B*). These results suggest a combination of presynaptic and postsynaptic alterations at inhibitory synapses. The above findings on mEPSC and mIPSC further indicate that W246G ELOVL4 mutation has opposite effects on net excitatory and inhibitory synaptic drives on Purkinje cells.

The W246G ELOVL4 mutation impairs short-term synaptic plasticity at the climbing fiber to Purkinje cell synapse

Purkinje cells receive two major excitatory inputs, those from parallel fibers which are axons of cerebellar granule cells and from climbing fibers that arise from the inferior olive. In order to understand whether the deficiency of excitatory synaptic transmission that we observed was present at both parallel fiber-Purkinje cell (PF-PC) and climbing fiber-Purkinje cell (CF-PC) synapses or was synapse specific, we recorded evoked EPSCs from Purkinje cells following stimulation of either input. We evaluated short-term synaptic plasticity at these synapses as

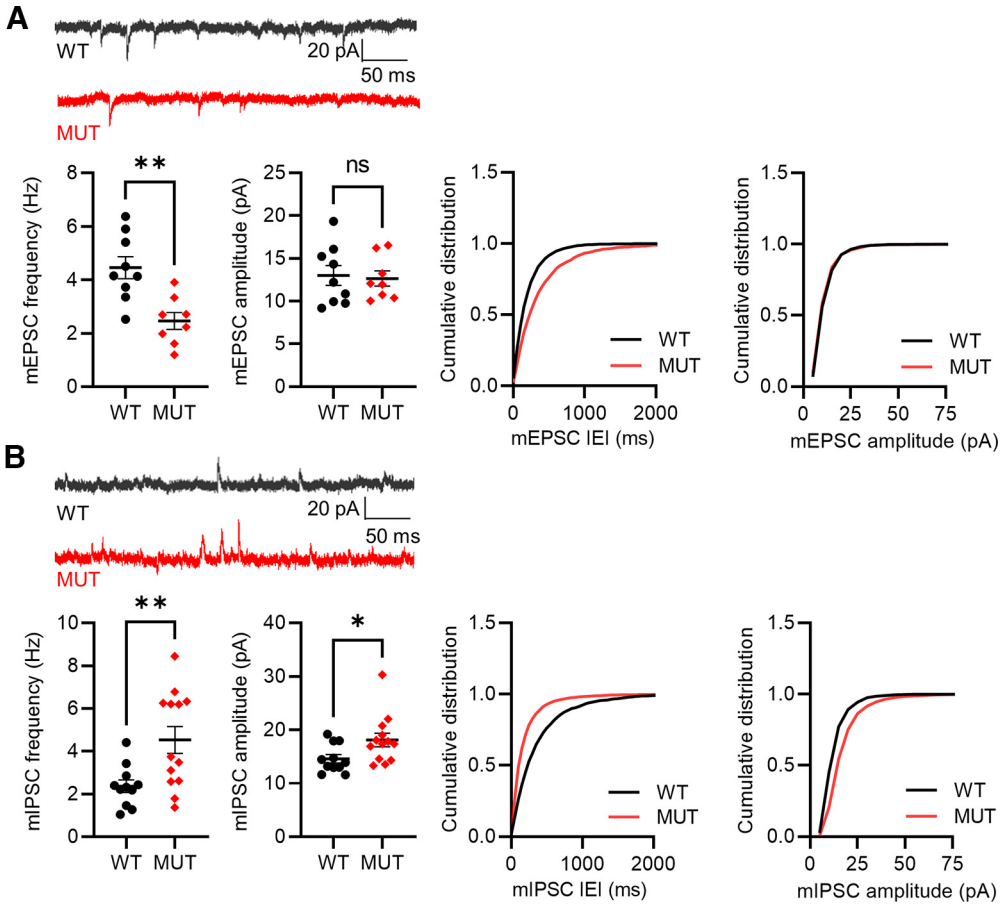

Figure 1. mEPSC and mIPSC are altered in Purkinje cells of W246G mutant ELOVL4 (MUT) rats. ***A***, The mean frequency (left graph) of mEPSC is reduced in MUT Purkinje cells, with no change in mean amplitude (center left graph). Cumulative distribution of interevent interval (IEI) of mEPSC shows rightward shift in MUT Purkinje cells (center right graph), with no change in the cumulative distribution of mEPSC amplitude (right graph). Example traces of mEPSC recordings are shown above the graphs (WT, black; MUT, red). $n = 8$–9 cells per group. ***B***, The mean frequency (left graph) and amplitude (center left graph) of mIPSC are increased in MUT Purkinje cells. Cumulative distribution of interevent interval (IEI) of mIPSC shows leftward shift (center right graph), and the cumulative distribution of mIPSC amplitude shows rightward shift (right graph) in MUT Purkinje cells. Example traces of mIPSC recordings are shown above the graphs (WT, black; MUT, red). $n = 11$–13 cells per group. Graphs show mean ± SEM along with individual data points in this and subsequent figures. *$p < 0.05$, **$p < 0.01$.

disturbances in these measures reflect alterations in functional properties of neurotransmitter release from the presynaptic terminal as opposed to changes in synapse number (Zucker and Regehr, 2002; Regehr, 2012). The pattern of changes in short-term plasticity also allow identification of the underlying physiological defect in neurotransmitter release (Schneggenburger et al., 2002; Baldelli et al., 2007; Lou et al., 2012; Thanawala and Regehr, 2016; Kaeser and Regehr, 2017).

CF-PC synapses undergo paired-pulse depression when two stimuli are presented close together (Hashimoto and Kano, 1998). We tested paired-pulse ratio at CF-PC synapses in WT and MUT slices by evoking EPSCs at interstimulus intervals (ISIs) of 20, 50, 100, 200 and 500 ms. The paired-pulse ratio was significantly increased in MUT cells at 20-, 50-, 100-, 200-, and 500-ms ISI (20 ms WT: 0.51 ± 0.03 vs MUT 0.61 ± 0.01 $p = 0.007$, 50 ms WT: 0.66 ± 0.02 vs MUT 0.76 ± 0.01 $p = 0.0003$, 100 ms WT: 0.72 ± 0.02 vs MUT 0.83 ± 0.02 $p = 0.0008$, 200 ms WT: 0.77 ± 0.02 vs MUT 0.84 ± 0.01 $p = 0.004$, 500 ms WT: 0.81 ± 0.02 vs MUT 0.88 ± 0.01 $p = 0.011$, $n = 12$ cells, 6 rats for WT; $n = 11$ cells, 3 rats for MUT; Fig. 2*A*), indicating reduced paired-pulse depression. As paired-pulse ratio is widely used as a measure of release probability and is inversely proportional to it (Dobrunz and Stevens, 1997; Regehr, 2012), our results suggest that CF-PC synapses have reduced release probability in MUT animals. To further dissect functional presynaptic defects, we recorded responses from CF-PC synapses following high-frequency climbing fiber stimulation at 20 and 50 Hz. In WT slices, EPSCs underwent prominent depression in response to 20-Hz stimulation and stabilized at a plateau later in the train (Fig. 2*B*). In contrast, there was reduced depression in MUT slices at $EPSC^2$ (in alignment with paired-pulse data), and also later in the train with EPSCs stabilizing at a significantly higher amplitude than WT (two-way ANOVA genotype × stimulation number interaction: $F_{(29,493)} = 5.941$, $p < 0.0001$; WT $n = 9$ cells, 4 rats; MUT $n = 10$ cells, 3 rats; Fig. 2*B*). Importantly, the difference between WT and MUT responses was larger at $EPSC^{30}$ than at $EPSC^2$ (WT: 0.49 ± 0.04 vs MUT 0.34 ± 0.05 $p = 0.018$; WT $n = 9$ cells, 4 rats; MUT $n = 10$ cells, 3 rats; Fig. 2*C*), which suggests the existence of a larger readily releasable pool of vesicles to sustain synaptic transmission under high frequency at CF-PC synapses in MUT slices (Regehr, 2012; Thanawala and Regehr, 2016). In response to 50-Hz stimulation, EPSCs in WT slices underwent robust depression nearing zero amplitude later in the train (Fig. 2*D*). The CF-PC synapses in MUT slices responded differently with significantly reduced depression at $EPSC^2$ (in alignment with paired-pulse data) and early parts of the train (two-way ANOVA genotype × stimulation number interaction: $F_{(29,493)} = 9.336$, $p < 0.0001$; WT $n = 9$ cells, 4 rats; MUT $n = 10$ cells, 3 rats; Fig. 2*D*). However, the EPSCs were similarly reduced later in the train in MUT slices as WT, suggesting that under extreme

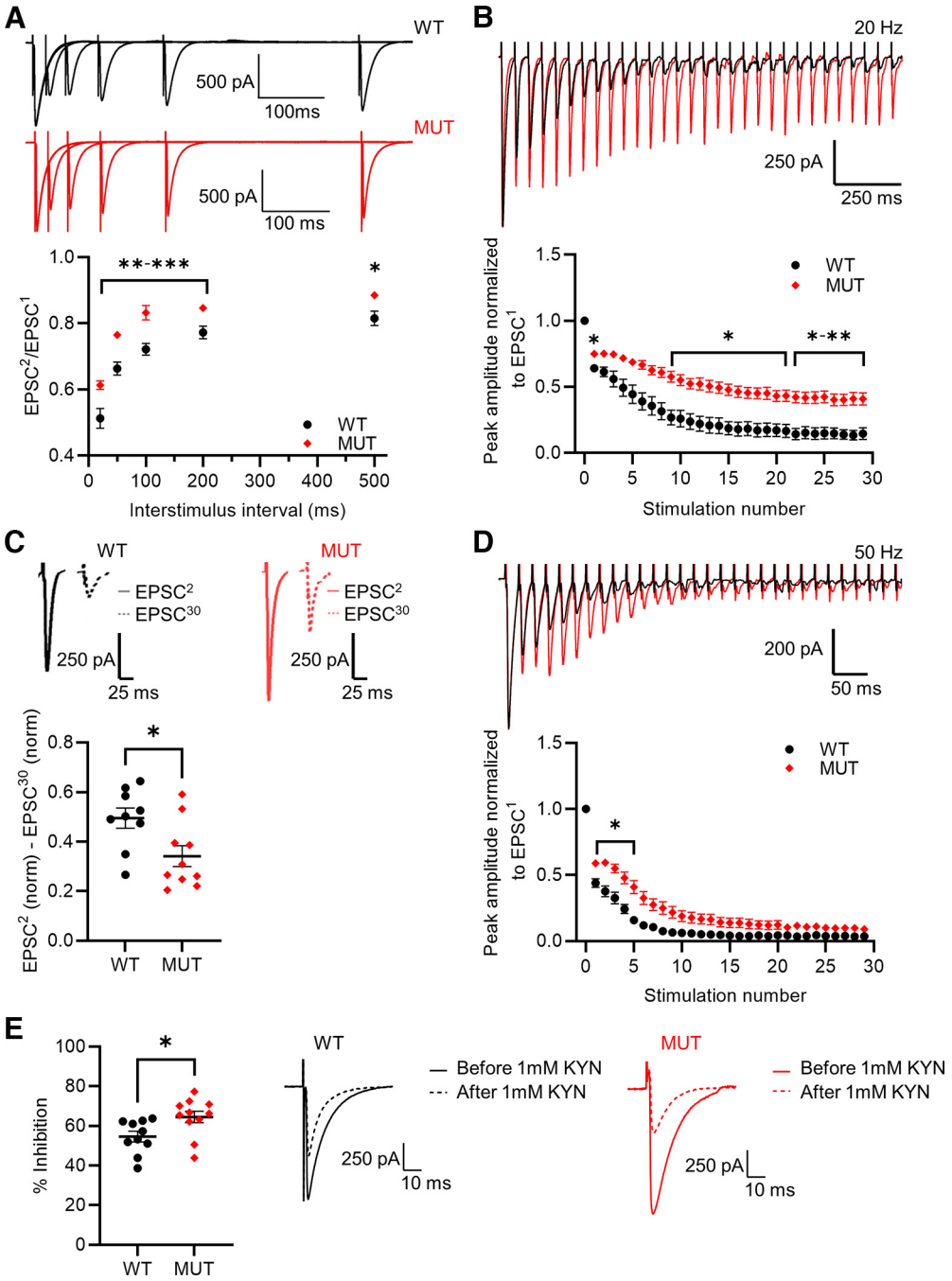

Figure 2. Short-term synaptic plasticity is impaired at climbing fiber-Purkinje cell (CF-PC) synapses in MUT cerebellum. ***A***, Paired-pulse ratio of EPSC amplitude at CF-PC synapses is increased in MUT cerebellum. Graph shows the mean paired-pulse ratio of EPSC amplitudes ($EPSC^2/EPSC^1$) from paired stimulation at 20-, 50-, 100-, 200-, and 500-ms interstimulus intervals. Example traces (WT, black; MUT, red) of averaged EPSCs from paired stimulation are shown above the graph. $n = 11$–12 cells per group. ***B***, Reduced decrement of EPSC amplitude in response to 20-Hz stimulation at CF-PC synapses in MUT cerebellum. Example traces (top; WT, black; MUT, red) and graph (bottom) showing peak EPSC amplitude at each stimulus in the 20-Hz train normalized to the amplitude of $EPSC^1$. $n = 9$–10 cells per group. ***C***, Mean subtracted value of second and 30th EPSC (bottom, graph) and example traces (top) depicting impaired decrement of EPSC amplitude during the 20-Hz train at MUT CF-PC synapses. ***D***, Reduced decrement of EPSC amplitude in early part of 50-Hz stimulation at CF-PC synapses in MUT cerebellum. Example traces (top; WT, black; MUT, red) and graph (bottom) showing peak EPSC amplitude at each stimulus in the 50-Hz train normalized to the amplitude of $EPSC^1$. $n = 9$–10 cells per group. Extended Data Figure 2-1 shows the quantification of release probability (P_r) and readily releasable pool size (RRP) obtained from the cumulative amplitude of CF-PC EPSC in response to depleting 50-Hz train. ***E***, Enhanced suppression of CF-PC EPSC by Kynurenic acid (KYN, 1 mM) in MUT cerebellum. Graph shows percentage inhibition of CF-PC EPSC by KYN. Example traces of EPSC from before (solid line) and after exposure to 1 mM KYN (dotted line) are shown on the right side of the graph. $n = 10$–11 cells per group. $^*p < 0.05$, $^{**}p < 0.01$, $^{***}p < 0.001$.

conditions of depletion, the larger pool size in MUT CF-PC synapses is not sufficient to sustain synaptic transmission. Since CF-PC synapses underwent similar depletion in the later parts of the 50-Hz train in WT and MUT slices, we used the data to calculate the quantal parameters. We plotted the cumulative amplitude of EPSCs and fit the curves with a linear regression extrapolating to the *y*-axis to quantify release probability (P_r) and size of the readily releasable pool (RRP), in accordance with the Schneggenburger–Neher method (Schneggenburger et al., 1999, 2002; Extended Data Fig. 2-1*A*). The quantification shows that P_r is significantly reduced in MUT CF-PC synapses compared with WT, in

agreement with our paired-pulse data (WT 0.40 ± 0.04, $n = 9$ cells, 4 rats; MUT 0.25 ± 0.02, $n = 10$ cells, 3 rats; $p = 0.001$; Extended Data Fig. 2-1*B*). In addition, RRP size is increased in MUT CF-PC synapses, which could contribute to reduced depression under high-frequency stimulation (WT 1639.04 ± 115.47 nA, $n = 9$ cells, 4 rats; MUT 2995.88 ± 340.27 nA, $n = 10$ cells, 3 rats; $p = 0.002$; Extended Data Fig. 2-1*C*).

In order to further evaluate neurotransmitter release at CF-PC synapses in MUT slices, we made use of kynurenic acid, which is a competitive, low affinity inhibitor of ionotropic glutamate receptors. The percentage inhibition achieved by kynurenic acid is inversely proportional to the amount of glutamate released at synapses (Beeson et al., 2020). We found that bath application of 1 mM kynurenic acid reduced EPSC size significantly more in MUT cells compared with WT (WT 54.62 ± 2.68%, $n = 10$ cells, 6 rats; MUT 64.50 ± 2.92%, $n = 11$ cells, 5 rats; $p = 0.023$; Fig. 2*E*). This suggests that less glutamate is released per CF-PC synapse onto MUT Purkinje cells and complements the findings above of reduced P_r at this synapse in MUT slices.

The W246G ELOVL4 mutation impairs short-term synaptic plasticity at the parallel fiber to Purkinje cell synapse

We next investigated whether the short-term synaptic plasticity is altered at PF-PC synapses in cerebellar slices from MUT rats. PF-PC synapses undergo paired-pulse facilitation when two stimuli are presented together (Atluri and Regehr, 1996). We evaluated paired-pulse facilitation at PF-PC synapses in WT and MUT slices by evoking EPSCs at interstimulus intervals (ISIs) of 20, 50, 100, 200, and 500 ms. The paired-pulse ratio was significantly reduced in MUT cells at 20-, 50-, and 100-ms ISI (20 ms WT: 1.96 ± 0.08 vs MUT 1.63 ± 0.06 $p = 0.003$, 50 ms WT: 1.80 ± 0.11 vs MUT 1.48 ± 0.05 $p = 0.009$, 100 ms WT: 1.47 ± 0.08 vs MUT 1.27 ± 0.03 $p = 0.021$, $n = 14$ cells, 8 rats for WT; $n = 16$ cells, 4 rats for MUT; Fig. 3*A*), suggesting enhanced release probability at PF-PC synapses in MUT slices. We further examined presynaptic function by examining synaptic responses to high-frequency parallel fiber stimulation at 20 and 50 Hz (Fig. 3*B*,*D*). In WT slices, EPSCs first underwent facilitation which came back to baseline at the end of the 30-stimulus train. In contrast, the data from MUT slices showed reduced facilitation at $EPSC^2$, congruent with our paired-pulse recordings, followed by persistence of EPSC size with little decrement over the course of the train (two-way ANOVA genotype × stimulation number interaction: $F_{(29,522)} = 12.63$, $p < 0.0001$; WT $n = 19$ cells, 11 rats; MUT $n = 19$ cells, 7 rats; Fig. 3*B*). Importantly, the difference between WT and MUT responses was larger at $EPSC^{30}$ than at EPSC2 (WT: 0.89 ± 0.12 vs MUT 0.03 ± 0.13 $p < 0.0001$; WT $n = 19$ cells, 11 rats; MUT $n = 19$ cells, 7 rats; Fig. 3*C*), suggesting a larger pool of readily releasable vesicles to sustain synaptic transmission under high frequency at PF-PC synapses in MUT slices. In response to 50-Hz stimulation, EPSCs in WT slices underwent initial facilitation followed by plateauing to a level below the baseline (two-way ANOVA genotype × stimulation number interaction: $F_{(29,609)} = 2.30$, $p = 0.0002$; WT $n = 9$ cells, 3 rats; MUT $n = 13$ cells, 4 rats; Fig. 3*D*). The facilitation in MUT slices was reduced at $EPSC^2$ compared with WT, in alignment with the paired-pulse data. In the later part of the train, the EPSC amplitudes in WT and MUT cells plateaued at similar levels, substantially above zero amplitude. Since the PF-PC EPSCs showed significant facilitation during the train and decrement in EPSC sizes was incomplete, we could not apply the linear regression method (which requires efficient depletion to be valid) to calculate the quantal parameters at this synapse (Schneggenburger et al., 2002; Neher, 2015).

We further evaluated neurotransmitter release at PF-PC synapses in WT and MUT slices by examining inhibition of EPSC size following bath application of 1 mM kynurenic acid. Kynurenic acid reduced EPSC size significantly less in MUT cells compared with WT (WT 70.83 ± 1.95%, $n = 9$ cells, 4 rats; MUT 61.45 ± 3.00%, $n = 7$ cells, 3 rats; $p = 0.016$; Fig. 3*E*). This suggests that more glutamate is released per PF-PC synapse in MUT Purkinje cells, complementing the finding of elevated P_r from paired-pulse data at this synapse in MUT slices.

Intrinsic excitability of Purkinje cells is unchanged in MUT cerebellum

The functional output of neurons depends not only on their synaptic inputs but also on their intrinsic excitability. Defects in voltage-gated ion channels and intrinsic excitability of Purkinje cells have been reported in animal models of ataxia (Hoxha et al., 2018). In order to investigate whether the intrinsic electrical properties of Purkinje cells are altered in MUT cerebellum, we first recorded action potentials in these cells in response to current injections. These whole-cell current-clamp recordings were done in the presence of the $GABA_A$ receptor antagonist picrotoxin to remove any confounding effect of inhibitory synaptic transmission in limiting spike output. We found that MUT Purkinje cells responded with a similar number and pattern of action potentials as WT cells (Fig. 4*A*). The number of action potentials in WT and MUT Purkinje cells at different levels of current injections ranging from 100 to 1000 pA were: 100 pA WT: 7.73 ± 1.03 vs MUT 8.90 ± 1.63 $p = 0.882$, 200 pA WT: 14.60 ± 1.61 vs MUT 15.83 ± 2.22 $p = 0.635$, 300 pA WT: 20.60 ± 2.09 vs MUT 22.07 ± 2.60 $p = 0.512$, 400 pA WT: 25.80 ± 2.48 vs MUT 27.60 ± 3.12 $p = 0.434$, 500 pA WT: 30.47 ± 2.88 vs MUT 32.20 ± 3.59 $p = 0.381$, 600 pA WT: 34.40 ± 3.19 vs MUT 36.27 ± 3.87 $p = 0.347$, 700 pA WT: 37.67 ± 3.46 vs MUT 39.57 ± 4.31 $p = 0.285$, 800 pA WT: 41.67 ± 4.59 vs MUT 42.40 ± 5.23 $p = 0.381$, 900 pA WT: 44.33 ± 4.92 vs MUT 45.17 ± 6.32 $p = 0.569$, 1000 pA WT: 46.50 ± 5.20 vs MUT 47.75 ± 6.68 $p = 0.476$, $n = 5$ cells, 2 rats for WT; $n = 6$ cells, 2 rats for MUT (Fig. 4*A*). This result suggests that the intrinsic ability of action potential generation is not altered in MUT Purkinje cells. In order to further evaluate intrinsic active properties of Purkinje cells, we examined I_h currents, which are important determinants of neuronal excitability (He et al., 2014). To this end, we injected hyperpolarization currents (ranging from −50 to −250 pA) in whole-cell current-clamp recordings, and measured the amplitude of depolarization sag that is generated by I_h currents. We found that the amplitude of depolarization sag was similar in WT and MUT Purkinje cells (−50 pA WT: 2.21 ± 0.34 mV vs MUT 2.42 ± 0.67 mV $p = 0.802$, −100 pA WT: 4.29 ± 0.54 mV vs MUT 5.02 ± 1.16 mV $p = 0.605$, −150 pA WT: 6.34 ± 0.88 mV vs MUT 7.21 ± 1.68 mV $p = 0.670$, −200 pA WT: 8.19 ± 0.75 mV vs MUT 9.21 ± 1.98 mV $p = 0.659$, −250 pA WT: 9.62 ± 1.14 mV vs MUT 11.03 ± 2.27 mV $p = 0.611$, $n = 6$ cells, 2 rats for WT; $n = 7$ cells, 2 rats for MUT; Fig. 4*B*). We then directly measured I_h currents in whole-cell voltage-clamp mode and observed that I_h current was unchanged in MUT Purkinje cells (−70 mV WT: 75.11 ± 5.45 pA vs MUT 75.97 ± 7.70 pA $p = 0.931$, −80 mV WT: 186.97 ± 12.79 pA vs MUT 163.36 ± 9.80 pA $p = 0.165$, −90 mV WT: 298.49 ± 21.43 pA vs MUT 253.10 ± 13.83 pA $p = 0.094$, −100 mV WT: 378.68 ± 23.96 pA vs MUT

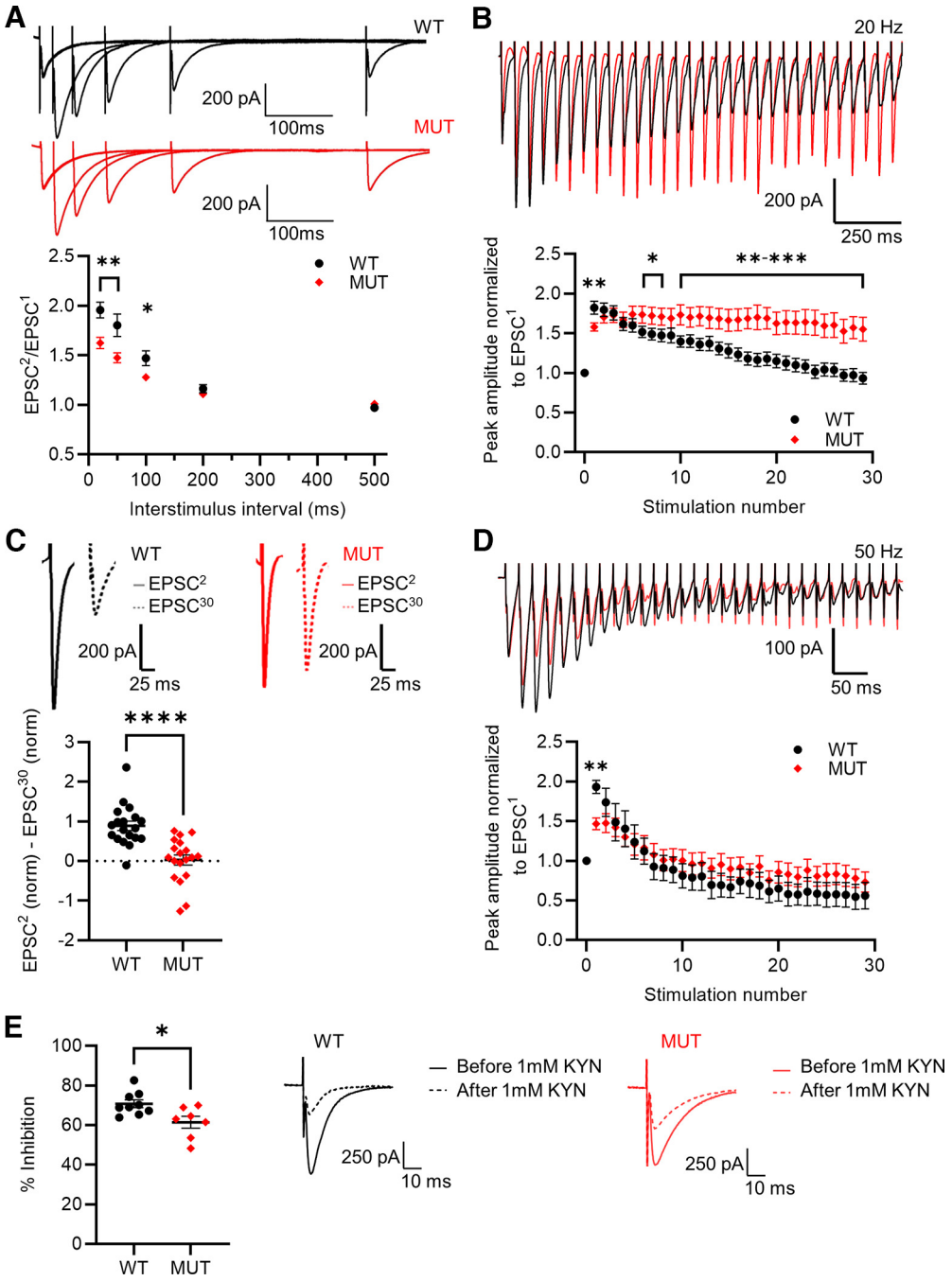

Figure 3. Short-term synaptic plasticity is impaired at parallel fiber-Purkinje cell (PF-PC) synapses in MUT cerebellum. ***A***, Paired-pulse ratio of EPSC amplitude at PF-PC synapses is decreased in MUT cerebellum. Graph shows the mean paired-pulse ratio of EPSC amplitudes ($EPSC^2/EPSC^1$) from paired stimulation at 20-, 50-, 100-, 200-, and 500-ms interstimulus intervals. Example traces (WT, black; MUT, red) of averaged EPSCs from paired stimulation are shown above the graph. $n = 14$–16 cells per group. ***B***, Reduced decrement of EPSC amplitude in response to 20-Hz stimulation at PF-PC synapses in MUT cerebellum. Example traces (top; WT, black; MUT, red) and graph (bottom) showing peak EPSC amplitude at each stimulus in the 20-Hz train normalized to the amplitude of $EPSC^1$. $n = 19$ cells per group. ***C***, Mean subtracted value of second and 30th EPSC (bottom, graph) and example traces (top) depicting impaired decrement of EPSC amplitude during the 20-Hz train at MUT PF-PC synapses. ***D***, Similar decrement of EPSC amplitude during 50-Hz stimulation at PF-PC synapses in WT and MUT cerebellum. Example traces (top; WT, black; MUT, red) and graph (bottom) showing peak EPSC amplitude at each stimulus in the 50-Hz train normalized to the amplitude of $EPSC^1$. $n = 9$–13 cells per group. ***E***, Reduced suppression of PF-PC EPSC by KYN (1 mM) in MUT cerebellum. Graph shows percentage inhibition of PF-PC EPSC by KYN. Example traces of EPSC from before (solid line) and after exposure to 1 mM KYN (dotted line) are shown on the right side of the graph. $n = 7$–9 cells per group. $^*p < 0.05$, $^{**}p < 0.01$, $^{***}p < 0.001$.

324.08 ± 25.69 pA $p = 0.153$, −110 mV WT: 474.75 ± 65.69 pA vs MUT 364.04 ± 32.34 pA $p = 0.141$, −120 mV WT: 514.55 ± 74.89 pA vs MUT 449.51 ± 60.44 pA $p = 0.508$, $n = 6$ cells, 2 rats for WT; $n = 7$ cells, 2 rats for MUT; Fig. 4*C*). Finally, we calculated the input resistance of Purkinje cells and found similar levels in WT and MUT slices (WT 52.55 ± 2.38 MΩ, $n = 14$ cells, 4 rats; MUT 55.98 ± 2.38 MΩ, $n = 14$ cells, 4 rats; $p = 0.317$; Fig. 4*D*). Overall, these results show that intrinsic excitability and electrical membrane properties are unaltered in the Purkinje cells of MUT cerebellum.

The density of dendritic spines is reduced in MUT Purkinje cells

We complemented our analysis of synaptic function in WT and MUT Purkinje cells with structural investigation of dendritic

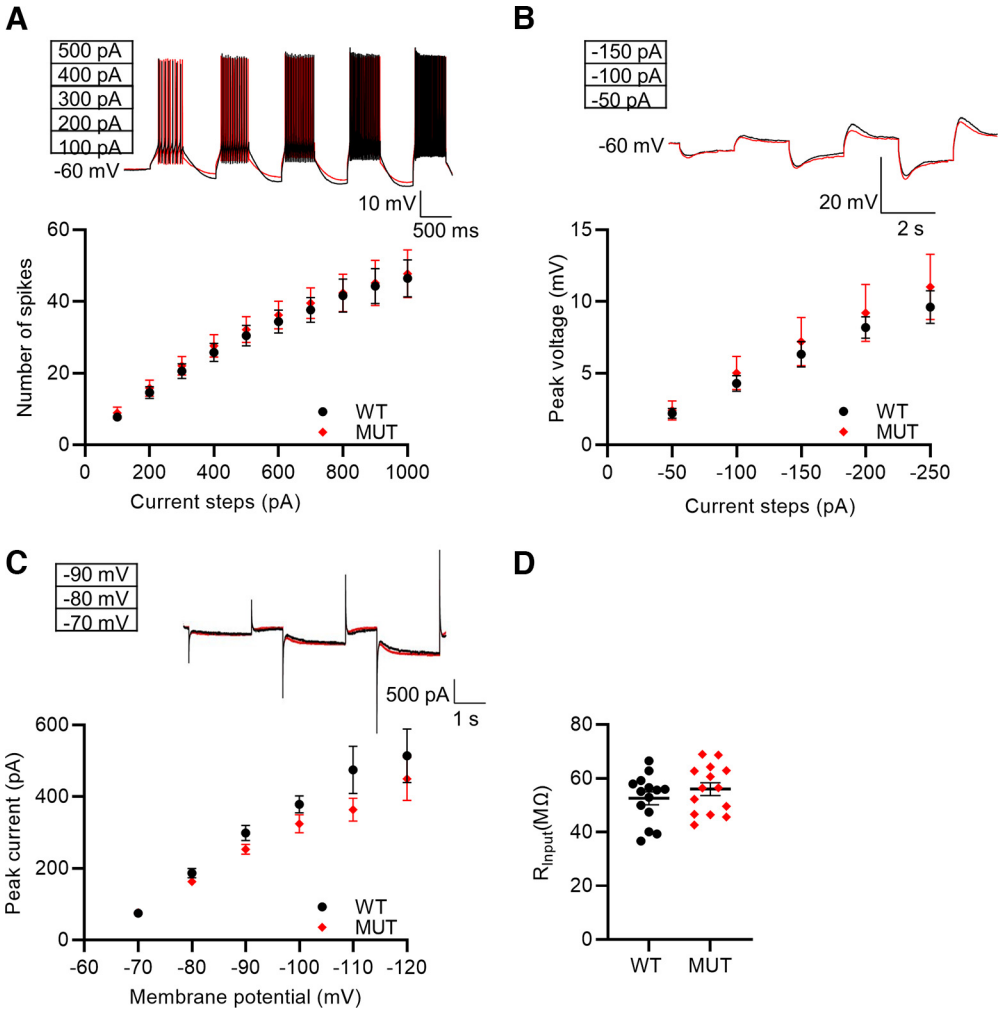

Figure 4. Intrinsic excitability of Purkinje cells is unaltered in MUT Purkinje cells. ***A***, The number of action potentials generated in Purkinje cells in response to current injection is similar in WT and MUT cerebellum. The graph shows the number of spikes that were induced in Purkinje cells in current-clamp mode, in response to 0.5-s-long current steps from 100–1000 pA in 100-pA increments. The example traces (WT, black; MUT, red) are shown above the graph. $n = 5$–6 cells/group. ***B***, The depolarization sag (recorded in current-clamp mode), mediated by I_h currents, is unchanged in MUT Purkinje cells. The graph shows the mean depolarization sag in response to 2-s-long negative current steps from −50 to −250 pA in −50-pA increments. The example traces (WT, black; MUT, red) are shown above the graph. $n = 6$–7 cells/group. ***C***, The I_h currents (recorded in voltage-clamp mode) are similar in WT and MUT Purkinje cells. The graph depicts the mean peak current (I_h) in response to 2-s-long hyperpolarizing voltage steps from −70 to −120 mV in −10-mV increments. The example traces (WT, black; MUT, red) are shown above the graph. $n = 6$–7 cells/group. ***D***, The input resistance (R_{input}) is unaltered in MUT Purkinje cells. Graph shows mean input resistance from Purkinje cells recorded in voltage-clamp mode with a K^+-based pipette solution. $n = 14$ cells/group.

spines. The parallel and climbing fibers form excitatory synapses onto spines, thus a change in their number could alter the excitatory drive on Purkinje cells. Because we observed a decrease in the excitatory drive in the form of reduced mEPSC frequency in MUT Purkinje cells, we investigated whether there is a change in the density of spines that might contribute to this decrease. We filled Purkinje cells with the fluorescent dye Alexa 568 hydrazide (0.5 mM) in whole-cell patch-clamp pipette, which effectively labeled the dendritic shafts and spines (Fig. 5*A*). The images from filled cells obtained on a spinning-disk confocal microscope revealed a reduction in the density of dendritic spines in MUT Purkinje cells compared with the WT. This was true both when individual segments isolated from cells were compared in WT and MUT slices (WT 1.95 ± 0.01 spines/μm, $n = 90$ segments, 10 cells, 2 rats; MUT 1.88 ± 0.01 spines/μm, $n = 90$ segments, 10 cells, 2 rats; $p = 0.004$; Fig. 5*A*), and when values from dendritic segments were averaged to obtain a single value for each cell (WT 1.95 ± 0.02 spines/μm, $n = 10$ cells, 2 rats; MUT 1.88 ± 0.01 spines/μm, $n = 10$ cells, 2 rats; $p = 0.006$; Fig. 5*A*). In parallel, we analyzed Purkinje cell spine density in the molecular layer of cerebellum using immunohistochemical staining for Calbindin, a marker of Purkinje cell dendrites (Ishikawa et al., 1995). Similar to our findings from cell filling, spine density was reduced in the molecular layer of cerebellum in MUT rats compared with WT animals (WT 17.26 ± 0.19 spines/10 μm, $n = 112$ dendritic segments, 6 rats; MUT 15.62 ± 0.27 spines/10 μm, $n = 106$ dendritic segments, 5 rats; $p = 0.0001$; Fig. 5*B*). The observed decrease in spine density, though modest, would contribute to the reduction in excitatory synaptic drive on MUT Purkinje cells (Fig. 1*A*) and aligns with other reports of altered spine density in animal models and patients with ataxia (Shintaku and Kaneda, 2009; Gao et al., 2011; Sugawara et al., 2013).

Discussion

The findings reported here elucidate the physiological mechanisms that are impaired at Purkinje cell synapses to generate

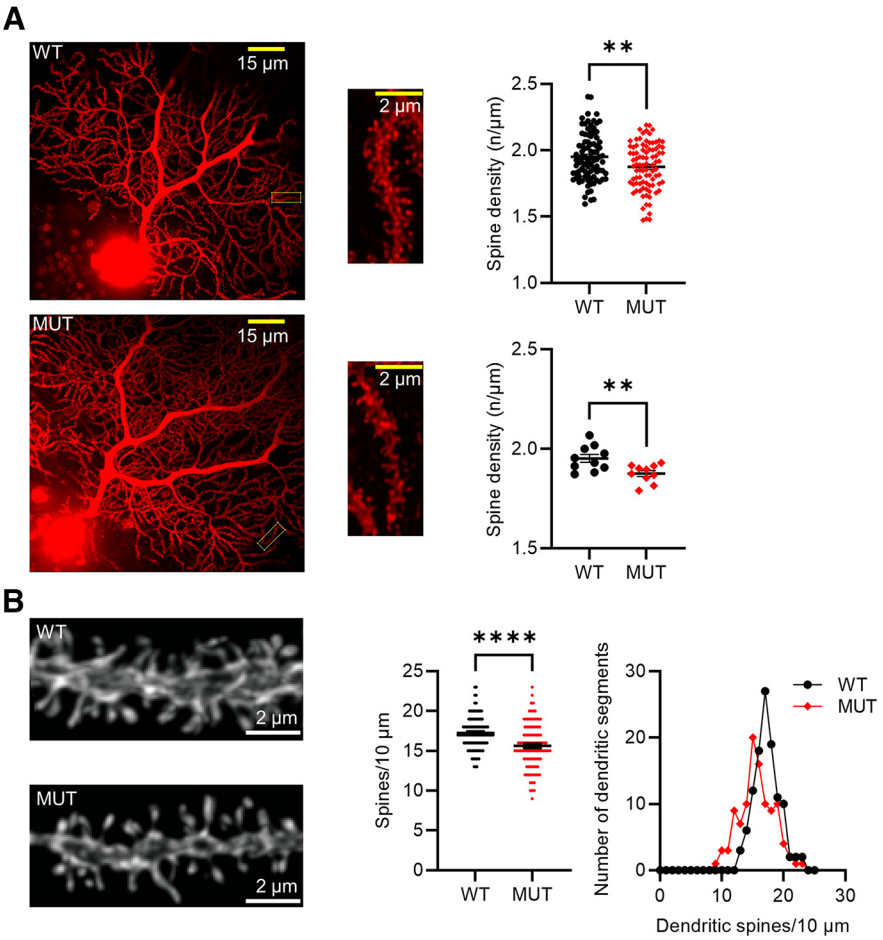

Figure 5. Dendritic spine density is reduced in MUT Purkinje cells. ***A***, The density of spines in Purkinje cells filled with Alexa 568 hydrazide is reduced in MUT cerebellum. Top graph shows the mean spine density, quantified from individual dendritic segments. Bottom graph shows the mean spine density obtained from averaged values for each cell. The example images from WT and MUT Purkinje cells filled with Alexa 568 hydrazide are shown on the left of the graphs at low and high magnification. $n = 90$ dendritic segments, 10 cells per group. ***B***, Immunohistochemical staining of calbindin shows reduced spine density in the molecular layer of MUT cerebellum. Graphs shows the mean spine density (left) and the distribution of spine density (right) in dendritic segments. The example images of sections labeled with calbindin antibody are shown on the left of the graphs. $n = 106–112$ dendritic segments per group. $^{**}p < 0.01$, $^{****}p < 0.0001$.

defects in synaptic transmission and plasticity in a rat model of SCA34 that harbors the ELOVL4 W246G mutation. Importantly, we find that these impairments are input-specific at excitatory and inhibitory synapses on MUT Purkinje cells.

We observed a distinct combination of changes in presynaptic physiology at the CF-PC and PF-PC synapses in MUT cerebellum, which included both divergent and similar alterations at these two sets of excitatory synapses. The MUT CF-PC synapses showed reduced paired-pulse depression during paired-pulse and high-frequency stimulation. Since the paired-pulse ratio is inversely proportional to P_r (Dobrunz and Stevens, 1997; Regehr, 2012), these results suggest that P_r is reduced at the CF-PC synapse in MUT cerebellum. This conclusion is complemented by the finding of stronger inhibition of CF-PC EPSCs by kynurenic acid in MUT slices that reflects reduced glutamate release per synapse. We further confirmed and quantified this decrease in P_r by using the linear regression method on the cumulative distribution of EPSC amplitudes from 50-Hz train. In contrast to these results, we found that P_r appears to be elevated at PF-PC synapses in MUT cerebellum. The MUT slices showed reduced paired-pulse facilitation at these synapses during paired-pulse and high-frequency stimulation, which suggests an increase in P_r. This was accompanied by a lower percentage inhibition of EPSC amplitude by kynurenic acid, further confirming enhanced glutamate release per PF-PC synapse in MUT cerebellum.

The results from high-frequency stimulation experiments revealed additional changes in presynaptic physiology apart from P_r. At MUT CF-PC synapses, there was reduced depression of EPSC size during 20-Hz stimulation such that the EPSCs plateaued at a much higher level than WT. This result could, in principle, be explained by a reduced basal P_r; however, the difference between WT and MUT EPSC sizes was much larger at the end of the 30-stimulus train than at EPSC^2, suggesting additional changes such as more efficient vesicle recycling and/or elevated RRP. Interestingly, the EPSCs at PF-PC synapses showed a similar pattern, with EPSCs persisting at higher amplitude during 20-Hz train in MUT Purkinje cells. This further strengthens the conclusion that reduced depletion in both CF-PC and PF-PC synapses in MUT cerebellum reflects alterations in vesicle dynamics in addition to alterations in P_r. In fact, the quantification of quantal parameters in robustly depleting CF-PC synapses using the linear regression method identified a larger RRP in MUT slices. Overall, these findings reveal that the ELOVL4 W246G mutation has opposite effects on P_r at CF-PC and PF-PC synapses, while effects on RRP are similar at these two sets of synapses.

Our analysis of mIPSCs in Purkinje cells uncovered for the first time the effect of an ELOVL4 mutation on inhibitory synaptic transmission. The results point toward a combination of presynaptic and postsynaptic defects at inhibitory synapses as we observed an increase in the frequency of mIPSCs along with elevated mIPSC amplitude in MUT Purkinje cells. The increase in mIPSC frequency likely reflects an elevated P_r at inhibitory synapses, which along with results from CF-PC and PF-PC synapses, suggests that alteration in P_r is a common theme across all synapse types on MUT Purkinje cells. The increase in mIPSC amplitude is likely because of changes in postsynaptic $GABA_A$ receptor content. Importantly, our studies identified a decrease in Purkinje cell spine density in MUT cerebellum, which together with mIPSC amplitude alteration suggests that synaptic defects in MUT are not restricted to presynaptic terminals but also extend to postsynaptic structures in Purkinje cells. In contrast to the change in mIPSC amplitude, the mEPSC amplitude is not changed, suggesting that the postsynaptic AMPA receptor content at remaining spines is likely not altered in MUT Purkinje cells. However, it should be noted that recent evidence indicates that even small-scale mislocalization of AMPA receptors within synaptic nanocolumns can impair synaptic transmission without altering mEPSC amplitude (Ramsey et al., 2021). Thus, more sophisticated super-resolution imaging will be needed in the future to dissect the postsynaptic AMPA receptor positioning in the MUT cerebellum. Interestingly, we did not observe any alterations in the intrinsic excitability of MUT Purkinje cells as the current injection-induced action potentials, input resistance, and I_h currents all were unchanged. This indicates that the predominant defect in the MUT cerebellum is synaptic dysfunction.

ELOVL4 catalyzes the biosynthesis of VLC-PUFA and VLC-SFA in a tissue-specific manner. While ELOVL4 primarily generates VLC-SFA in the brain and skin, the VLC-PUFA are the principal products in the retina and sperm (Hopiavuori et al., 2019; Yeboah et al., 2021). We have recently shown that the W246G mutation in ELOVL4 impairs biosynthesis of 28:0–36:0 VLC-SFA from 24:0 precursor supplementation *in vitro*, while having minimal effect on VLC-PUFA biosynthesis (Gyening et al., 2023). Accordingly, W246G MUT rats have reduced levels of 28:0 and 30:0 in the skin but normal VLC-PUFA levels in retina (Agbaga et al., 2020; Yeboah et al., 2021). The selective deficiency of VLC-SFA in MUT rats suggests that the synaptic disturbances we report here are likely because of the deficiency of VLC-SFA. This is further supported by our previous work with mice carrying a homozygous 5-bp STGD3 deletion in *Elovl4*. Primary neuronal cultures derived from these animals demonstrated altered kinetics of neurotransmitter release that was rescued by supplementation with VLC-SFA (28:0 + 30:0) in the culture medium (Hopiavuori et al., 2018). In addition, lipidomic analysis on baboon hippocampus identified VLC-SFA enriched in synaptic vesicles with little detection of VLC-PUFA (Hopiavuori et al., 2018). Future work involving rescue with dietary or intrabrain administration of 28:0 and 30:0 will clarify the dependence of cerebellar synaptic defects on VLC-SFA deficiency in MUT rats.

How does VLC-SFA deficiency arising from W246G and other mutations in ELOVL4 may lead to the observed synaptic defects? Our findings of altered P_r at both CF-PC and PF-PC synapses, and likely at MLI-PC synapses (reflected in reduced mIPSC frequency) suggest an important role of VLC-SFA in regulating synaptic vesicle fusion at the active zone. The fusion of synaptic vesicles with the presynaptic plasma membrane is a complex multistep process that requires initial contact (docking), formation of a hemi-fused state, and completion of full fusion followed by retrieval of the membrane by endocytosis (Sudhof, 2004; Kaeser and Regehr, 2014). The VLC-SFA are enriched in synaptic vesicles as previously identified in the baboon hippocampus (Hopiavuori et al., 2018) and could potentially affect any of these steps in the synaptic vesicle cycle which are critically dependent on the lipid composition of the membranes (Rohrbough and Broadie, 2005). The long length of VLC-SFA could allow their acyl chains to traverse both leaflets of the vesicle lipid bilayer, thus affecting the van der Waals interactions of the lipids in the apposing membranes during vesicle fusion (Deák et al., 2019). Interestingly, the P_r is altered in opposite ways in CF-PC and PF-PC synapses, and we observed additional changes in presynaptic physiology that reflect alterations in RRP size. This suggests that the VLC-SFA are not solely and simply acting as barriers in synaptic vesicle fusion but function as critical regulators in multiple steps of vesicle cycle that could differ among different types of synapses. These functions may arise from actions of VLC-SFA in regulating the function of proteins involved in synaptic vesicle cycle through covalent/noncovalent interactions, organization of lipid rafts or modulation of signaling pathways. It is important to note here that in addition to presynaptic deficits, we also observed reduced density of dendritic spines in Purkinje cells in MUT rats. This suggests that VLC-SFA deficiency also leads to postsynaptic defects, underscoring pleiotropic roles of VLC-SFA at synapses.

How do the synaptic disturbances that we identified at Purkinje cell synapses lead to ataxia that is observed in MUT rats? Our results show a net decrease in basal excitatory drive on MUT Purkinje cells along with an increase in inhibitory transmission. These changes are likely to suppress Purkinje cell output and thus impair their ability to provide instructive signals to deep cerebellar nuclei during motor activity. Interestingly, increased frequency and amplitude of spontaneous IPSC were reported in a mouse model of episodic ataxia 1 (Herson et al., 2003), which together with our findings advance the possibility that altered inhibitory synaptic transmission on Purkinje cells may be a common but underappreciated defect among many hereditary ataxias. Increased inhibition could also impair the induction of long-term depression (LTD) and long-term potentiation (LTP) at CF-PC and PF-PC synapses, which are critical for motor learning, and are impaired in MUT rats (Nagaraja et al., 2021). Apart from LTP and LTD, the short-term synaptic plasticity mediated by presynaptic changes in neurotransmitter release is also critical for information processing at synapses (Zucker and Regehr, 2002; Le Guen and De Zeeuw, 2010; Regehr, 2012). This is highly relevant to the function of Purkinje cells as precise interplay of PF-PC and CF-PC synaptic responses determines their output during motor activity and learning (De Zeeuw et al., 2021). Accordingly, disturbances in cerebellar short-term synaptic plasticity in knock-out mice lacking Munc13-3 (Augustin et al., 2001) or mGluR4 (Pekhletski et al., 1996) are associated with ataxia, even in the absence of detectable changes in long-term synaptic plasticity. Our finding of major alterations in short-term synaptic plasticity in MUT cerebellum uncovers a previously unrecognized substrate for dysfunction of Purkinje cell activity and ataxia in an SCA34 model. Future work involving in vivo recordings combined with optogenetic manipulations would address the causal contribution of the synaptic impairments reported here to the motor incoordination displayed by MUT rats.

References

Adibhatla RM, Hatcher JF (2007) Role of lipids in brain injury and diseases. Future Lipidol 2:403–422.

Agbaga MP, Brush RS, Mandal MN, Henry K, Elliott MH, Anderson RE (2008) Role of Stargardt-3 macular dystrophy protein (ELOVL4) in the biosynthesis of very long chain fatty acids. Proc Natl Acad Sci U S A 105:12843–12848.

Agbaga MP, Stiles MA, Brush RS, Sullivan MT, Machalinski A, Jones KL, Anderson RE, Sherry DM (2020) The Elovl4 spinocerebellar Ataxia-34 mutation 736T>G (p.W246G) impairs retinal function in the absence of photoreceptor degeneration. Mol Neurobiol 57:4735–4753.

Ahmad M, Polepalli JS, Goswami D, Yang X, Kaeser-Woo YJ, Südhof TC, Malenka RC (2012) Postsynaptic complexin controls AMPA receptor exocytosis during LTP. Neuron 73:260–267.

Aldahmesh MA, Mohamed JY, Alkuraya HS, Verma IC, Puri RD, Alaiya AA, Rizzo WB, Alkuraya FS (2011) Recessive mutations in ELOVL4 cause ichthyosis, intellectual disability, and spastic quadriplegia. Am J Hum Genet 89:745–750.

Alessenko AV, Albi E (2020) Exploring sphingolipid implications in neurodegeneration. Front Neurol 11:437.

Atluri PP, Regehr WG (1996) Determinants of the time course of facilitation at the granule cell to Purkinje cell synapse. J Neurosci 16:5661–5671.

Augustin I, Korte S, Rickmann M, Kretzschmar HA, Südhof TC, Herms JW, Brose N (2001) The cerebellum-specific Munc13 isoform Munc13-3 regulates cerebellar synaptic transmission and motor learning in mice. J Neurosci 21:10–17.

Baldelli P, Fassio A, Valtorta F, Benfenati F (2007) Lack of synapsin I reduces the readily releasable pool of synaptic vesicles at central inhibitory synapses. J Neurosci 27:13520–13531.

Beaudin M, Sellami L, Martel C, Touzel-Deschênes L, Houle G, Martineau L, Lacroix K, Lavallée A, Chrestian N, Rouleau GA, Gros-Louis F, Laforce R Jr, Dupré N (2020) Characterization of the phenotype with cognitive impairment and protein mislocalization in SCA34. Neurol Genet 6:e403.

Beeson KA, Beeson R, Westbrook GL, Schnell E (2020) $\alpha 2\delta$-2 protein controls structure and function at the cerebellar climbing fiber synapse. J Neurosci 40:2403–2415.

Bernstein PS, Tammur J, Singh N, Hutchinson A, Dixon M, Pappas CM, Zabriskie NA, Zhang K, Petrukhin K, Leppert M, Allikmets R (2001) Diverse macular dystrophy phenotype caused by a novel complex mutation in the ELOVL4 gene. Invest Ophthalmol Vis Sci 42:3331–3336.

Bourque PR, Warman-Chardon J, Lelli DA, LaBerge L, Kirshen C, Bradshaw SH, Hartley T, Boycott KM (2018) Novel ELOVL4 mutation associated with erythrokeratodermia and spinocerebellar ataxia (SCA 34). Neurol Genet 4:e263.

Cadieux-Dion M, Turcotte-Gauthier M, Noreau A, Martin C, Meloche C, Gravel M, Drouin CA, Rouleau GA, Nguyen DK, Cossette P (2014) Expanding the clinical phenotype associated with ELOVL4 mutation: study of a large French-Canadian family with autosomal dominant spinocerebellar ataxia and erythrokeratodermia. JAMA Neurol 71:470–475.

Deák F, Anderson RE, Fessler JL, Sherry DM (2019) Novel cellular functions of very long chain-fatty acids: insight from ELOVL4 mutations. Front Cell Neurosci 13:428.

De Zeeuw CI, Lisberger SG, Raymond JL (2021) Diversity and dynamism in the cerebellum. Nat Neurosci 24:160–167.

Di Paolo G, Kim TW (2011) Linking lipids to Alzheimer's disease: cholesterol and beyond. Nat Rev Neurosci 12:284–296.

Dobrunz LE, Stevens CF (1997) Heterogeneity of release probability, facilitation, and depletion at central synapses. Neuron 18:995–1008.

Dueñas AM, Goold R, Giunti P (2006) Molecular pathogenesis of spinocerebellar ataxias. Brain 129:1357–1370.

Edwards AO, Donoso LA, Ritter R 3rd (2001) A novel gene for autosomal dominant Stargardt-like macular dystrophy with homology to the SUR4 protein family. Invest Ophthalmol Vis Sci 42:2652–2663.

Fitzner D, Bader JM, Penkert H, Bergner CG, Su M, Weil MT, Surma MA, Mann M, Klose C, Simons M (2020) Cell-type- and brain-region-resolved mouse brain lipidome. Cell Rep 32:108132.

Gao Y, Perkins EM, Clarkson YL, Tobia S, Lyndon AR, Jackson M, Rothstein JD (2011) β-III spectrin is critical for development of Purkinje cell dendritic tree and spine morphogenesis. J Neurosci 31:16581–16590.

Gyening YK, Chauhan NK, Tytanic M, Ea V, Brush RS, Agbaga MP (2023) ELOVL4 mutations that cause spinocerebellar Ataxia-34 differentially alter very long chain fatty acid biosynthesis. J Lipid Res 64:100317.

Hashimoto K, Kano M (1998) Presynaptic origin of paired-pulse depression at climbing fibre-Purkinje cell synapses in the rat cerebellum. J Physiol 506:391–405.

He C, Chen F, Li B, Hu Z (2014) Neurophysiology of HCN channels: from cellular functions to multiple regulations. Prog Neurobiol 112:1–23.

Herson PS, Virk M, Rustay NR, Bond CT, Crabbe JC, Adelman JP, Maylie J (2003) A mouse model of episodic ataxia type-1. Nat Neurosci 6:378–383.

Hopiavuori BR, Deák F, Wilkerson JL, Brush RS, Rocha-Hopiavuori NA, Hopiavuori AR, Ozan KG, Sullivan MT, Wren JD, Georgescu C, Szweda L, Awasthi V, Towner R, Sherry DM, Anderson RE, Agbaga MP (2018) Homozygous expression of mutant ELOVL4 leads to seizures and death in a novel animal model of very long-chain fatty acid deficiency. Mol Neurobiol 55:1795–1813.

Hopiavuori BR, Anderson RE, Agbaga MP (2019) ELOVL4: very long-chain fatty acids serve an eclectic role in mammalian health and function. Prog Retin Eye Res 69:137–158.

Hoxha E, Balbo I, Miniaci MC, Tempia F (2018) Purkinje cell signaling deficits in animal models of ataxia. Front Synaptic Neurosci 10:6.

Hussain G, Wang J, Rasul A, Anwar H, Imran A, Qasim M, Zafar S, Kamran SKS, Razzaq A, Aziz N, Ahmad W, Shabbir A, Iqbal J, Baig SM, Sun T (2019) Role of cholesterol and sphingolipids in brain development and neurological diseases. Lipids Health Dis 18:26.

Ishikawa K, Mizusawa H, Fujita T, Ohkoshi N, Doi M, Komatsuzaki Y, Iwamoto H, Ogata T, Shoji S (1995) Calbindin-D 28k immunoreactivity in the cerebellum of spinocerebellar degeneration. J Neurol Sci 129:179–185.

Kaeser PS, Regehr WG (2014) Molecular mechanisms for synchronous, asynchronous, and spontaneous neurotransmitter release. Annu Rev Physiol 76:333–363.

Kaeser PS, Regehr WG (2017) The readily releasable pool of synaptic vesicles. Curr Opin Neurobiol 43:63–70.

Le Guen MC, De Zeeuw CI (2010) Presynaptic plasticity at cerebellar parallel fiber terminals. Funct Neurol 25:141–151.

Lou X, Fan F, Messa M, Raimondi A, Wu Y, Looger LL, Ferguson SM, De Camilli P (2012) Reduced release probability prevents vesicle depletion and transmission failure at dynamin mutant synapses. Proc Natl Acad Sci U S A 109:E515–E523.

Mir H, Raza SI, Touseef M, Memon MM, Khan MN, Jaffar S, Ahmad W (2014) A novel recessive mutation in the gene ELOVL4 causes a neuro-ichthyotic disorder with variable expressivity. BMC Med Genet 15:25.

Nagaraja RY, Sherry DM, Fessler JL, Stiles MA, Li F, Multani K, Orock A, Ahmad M, Brush RS, Anderson RE, Agbaga MP, Deák F (2021) W246G mutant ELOVL4 impairs synaptic plasticity in parallel and climbing fibers and causes motor defects in a rat model of SCA34. Mol Neurobiol 58:4921–4943.

Neher E (2015) Merits and limitations of vesicle pool models in view of heterogeneous populations of synaptic vesicles. Neuron 87:1131–1142.

Ozaki K, et al. (2015) A novel mutation in ELOVL4 leading to spinocerebellar ataxia (SCA) with the hot cross bun sign but lacking erythrokeratodermia: a broadened spectrum of SCA34. JAMA Neurol 72:797–805.

Ozaki K, Ansai A, Nobuhara K, Araki T, Kubodera T, Ishii T, Higashi M, Sato N, Soga K, Mizusawa H, Ishikawa K, Yokota T (2019) Prevalence and clinicoradiological features of spinocerebellar ataxia type 34 in a Japanese ataxia cohort. Parkinsonism Relat Disord 65:238–242.

Pekhletski R, Gerlai R, Overstreet LS, Huang XP, Agopyan N, Slater NT, Abramow-Newerly W, Roder JC, Hampson DR (1996) Impaired cerebellar synaptic plasticity and motor performance in mice lacking the mGluR4 subtype of metabotropic glutamate receptor. J Neurosci 16:6364–6373.

Ramsey AM, Tang AH, LeGates TA, Gou XZ, Carbone BE, Thompson SM, Biederer T, Blanpied TA (2021) Subsynaptic positioning of AMPARs by LRRTM2 controls synaptic strength. Sci Adv 7:eabf3126.

Regehr WG (2012) Short-term presynaptic plasticity. Cold Spring Harb Perspect Biol 4:a005702.

Rohrbough J, Broadie K (2005) Lipid regulation of the synaptic vesicle cycle. Nat Rev Neurosci 6:139–150.

Schneggenburger R, Meyer AC, Neher E (1999) Released fraction and total size of a pool of immediately available transmitter quanta at a calyx synapse. Neuron 23:399–409.

Schneggenburger R, Sakaba T, Neher E (2002) Vesicle pools and short-term synaptic depression: lessons from a large synapse. Trends Neurosci 25:206–212.

Sherry DM, Hopiavuori BR, Stiles MA, Rahman NS, Ozan KG, Deak F, Agbaga MP, Anderson RE (2017) Distribution of ELOVL4 in the developing and adult mouse brain. Front Neuroanat 11:38.

Shintaku M, Kaneda D (2009) Chromosome 16q22.1-linked autosomal dominant cerebellar ataxia: an autopsy case report with some new observations on cerebellar pathology. Neuropathology 29:285–292.

Sudhof TC (2004) The synaptic vesicle cycle. Annu Rev Neurosci 27:509–547.

Sugawara T, Hisatsune C, Le TD, Hashikawa T, Hirono M, Hattori M, Nagao S, Mikoshiba K (2013) Type 1 inositol trisphosphate receptor regulates cerebellar circuits by maintaining the spine morphology of Purkinje cells in adult mice. J Neurosci 33:12186–12196.

Thanawala MS, Regehr WG (2016) Determining synaptic parameters using high-frequency activation. J Neurosci Methods 264:136–152.

Troyano-Rodriguez E, Wirsig-Wiechmann CR, Ahmad M (2019a) Neuroligin-2 determines inhibitory synaptic transmission in the lateral septum to optimize stress-induced neuronal activation and avoidance behavior. Biol Psychiatry 85:1046–1055.

Troyano-Rodriguez E, Mann S, Ullah R, Ahmad M (2019b) PRRT1 regulates basal and plasticity-induced AMPA receptor trafficking. Mol Cell Neurosci 98:155–163.

Xiao C, Binkley EM, Rexach J, Knight-Johnson A, Khemani P, Fogel BL, Das S, Stone EM, Gomez CM (2019) A family with spinocerebellar ataxia and retinitis pigmentosa attributed to an ELOVL4 mutation. Neurol Genet 5: e357.

Yeboah GK, Lobanova ES, Brush RS, Agbaga MP (2021) Very long chain fatty acid-containing lipids: a decade of novel insights from the study of ELOVL4. J Lipid Res 62:100030.

Zhang K, Kniazeva M, Han M, Li W, Yu Z, Yang Z, Li Y, Metzker ML, Allikmets R, Zack DJ, Kakuk LE, Lagali PS, Wong PW, MacDonald IM, Sieving PA, Figueroa DJ, Austin CP, Gould RJ, Ayyagari R, Petrukhin K (2001) A 5-bp deletion in ELOVL4 is associated with two related forms of autosomal dominant macular dystrophy. Nat Genet 27:89–93.

Zucker RS, Regehr WG (2002) Short-term synaptic plasticity. Annu Rev Physiol 64:355–405.